Journal of Industrial and Engineering Chemistry 121 (2023) 489–498

Contents lists available at ScienceDirect

Journal of Industrial and Engineering Chemistry

journal homepage: www.elsevier.com/locate/jiec

High-performance cathode promoted by reduced graphene oxide nanofibers with well-defined interconnected meso-/micro pores for rechargeable Li-Se batteries

Chan Sic Kim [a], Rakesh Saroha [a], Hyun Ho Choi [a], Jang Hyeok Oh [a], Gi Dae Park [b,*], Dong-Won Kang [c,*], Jung Sang Cho [a,*]

[a] Department of Engineering Chemistry, Chungbuk National University, Chungdae-Ro Seowon-Gu, Cheongju-Si, Chungbuk, Republic of Korea
[b] Department of Advanced Materials Engineering, Chungbuk National University, Chungdae-Ro 1, Seowon-gu, Cheongju, Chungbuk 28644, Republic of Korea
[c] School of Energy Systems Engineering, Chung-Ang University, Seoul 06974, Republic of Korea

ARTICLE INFO

Article history:
Received 15 November 2022
Revised 19 January 2023
Accepted 5 February 2023
Available online 11 February 2023

Keywords:
Lithium-selenium battery
Electrospinning
Porous carbon host
Conductive matrix

ABSTRACT

Highly conductive nanostructures comprising one-dimensional (1D) reduced graphene oxide (rGO) nanofibers (NFs) and bimodal pores i.e., meso-/micropores, as efficient cathode hosts (Bi-P-rGO) for Li–Se batteries were prepared. The highly conductive rGO matrix acts as a self-supporting skeleton to enhance the structural integrity of the nanostructure besides providing numerous conducting pathways for rapid charge transfer. Moreover, highly interconnected chain-like mesopores guarantee efficient electrolyte percolation, whereas the micropores offer highly active material impregnation. Correspondingly, Bi-P-rGO@Se as a high-performance cathode was visualized, which demonstrated an overall enhanced electrochemical performance such as excellent rate capability (up to 20.0C) and overwhelming long-term cycling stability (73% capacity retention at the end of 800cycles with an average capacity decay rate of just 0.03% per cycle at 0.5C rate). The exceptional electrochemical performance of the Bi-P-rGO@Se cathode can be attributed to its highly porous structure, which promises efficient electrolyte infiltration and diffusion of charged species, high active material utilization within micropores, availability of conductive pathways for fast charge transfer, and high structural integrity. Therefore, we anticipate that the structural and electrochemical results presented in this work will provide significant insights into the synthesis of high-performance porous and conductive nanostructures for a wide range of applications.

Introduction

The state-of-the-art lithium–ion battery (LIB) technology ruled the portable electronics market since its introduction in 1990 by Sony Corporation mainly due to its high gravimetric energy density (~250 Wh kg^{-1}) and volumetric energy density (~700 Wh/L) [1–3]. Tremendous advances in the past few decades have allowed researchers to utilize LIBs to achieve full capacity in terms of energy density [4]. However, for commercial applications, such as large-scale grid storage or transportation systems that require even higher energy densities, new rechargeable systems are required [4–7]. In this scenario, the lithium–sulfur battery (LSB) technology conforms to the requirements of high gravimetric and volumetric energy density, low production cost due to sulfur abundance, and environmental friendliness [8–14]. However, LSBs still face commercial hindrances due to some fundamental issues, such as the insulating nature of elemental sulfur and discharge products, the well-known parasitic "shuttle effect," severe volumetric variations, and unstable Li anodes [15–19].

Selenium has attracted immense interest from the research community as a possible alternative to elemental S owing to its similarity to S in terms of electrochemical properties after its first introduction in 2012 by Amine et al. [20]. In addition, the volumetric capacity of Se-based cathodes (3253 mA h cm^{-3}) is comparable with S-based composites (3467 mA h cm^{-3}) with moderately high theoretical discharge capacity (675 mA h g^{-1}) [21]. Furthermore, Se is less reactive (i.e., has a lower proportion of side reactions) and can thus be controlled more easily during the electrochemical process [22]. Besides, the high electrical conductivity of Se (10^{-3} S m^{-1}) compared to S (10^{-28} S m^{-1}) is an additional advantage [23,24],

* Corresponding authors.
E-mail addresses: gdpark@chungbuk.ac.kr (G.D. Park), kangdwn@cau.ac.kr (D.-W. Kang), jscho@cbnu.ac.kr (J.S. Cho).

https://doi.org/10.1016/j.jiec.2023.02.004
1226-086X/

which makes Se an appropriate choice [25]. However, like LSBs, Li–Se batteries also suffer from polyselenide dissolution during the electrochemical processes. In addition, the low utilization of bulk Se, along with poor electron and ion transfer properties, results in substandard electrochemical performance [26].

Substantial research efforts have been made during the last decade to resolve these issues, which mainly include the impregnation of Se into porous hosts [23,26–30], advanced nanostructure morphologies (core–shell, 3D spheres, etc.) [31–35], freestanding architecture [36], and even modification of electrolytes [37]. For instance, Feng et al. reported synthesis of microporous carbon spheres (MPCS) and utilized them as Se-host *via* melt-diffusion method [28]. Likewise, Liu et al. prepared hierarchically porous soyabean-derived carbon as Se-host and investigate the electrochemical performance [38]. In particular, one-dimensional (1D) nanofibers (NFs) are highly preferable owing to their facile synthesis and easily controllable parameters that result in unique structural advantages that facilitate charge transport [39]. Additionally, the design of 1D porous nanofibers is highly desirable to accommodate elemental Se. The porous structure not only provides sufficient space for high-active-material impregnation but also increases the active contact area between Se and the electrolyte, thus reducing the effective diffusion length for charged species [40]. Moreover, to utilize a high proportion of active material, fast redox kinetics must be supported inside the 1D porous nanostructure. For instance, Wang et al. introduce Janus-type Se infiltrated porous N-doped carbon nanofibers decorated with $Ti_3C_2T_x$-MXene on top (PNCNFs/Se@MXene) for robust rate capabilities and long-term cycling stability [41].

Based on the above discussion, we utilized a 1D, highly porous, and conductive host for stable Li–Se batteries. The 1D framework was prepared *via* a traditional electrospinning technique. Porosity was incorporated using size-controlled polystyrene (PS) nanobeads (ϕ = 100 nm) and chemical activation using KOH. The decomposition of the PS nanobeads resulted in the formation of mesopores, whereas the KOH activation introduced micropores in the nanostructure. The mesopores accelerate the electrolyte infiltration process, whereas the micropores guarantee the impregnation of the active material in a high proportion. Furthermore, to enhance the overall conductivity of the nanostructure and rapid reaction kinetics for charge transfer, graphene oxide (GO) nanosheets were integrated and transformed into reduced graphene oxide (rGO) during post heat-treatment. The rGO also acts as a self-supporting matrix that enhances the structural integrity of the nanofibers during the redox process. The obtained rGO nanofibers comprising bimodal pores i.e., meso-/ micropores (Bi-P-rGO NFs), were further applied as efficient Se hosts to obtain high-performance Se cathodes (Bi-P-rGO@Se) using a well-known melt diffusion process.

Benefitting from the novel nanostructure design strategy, the Bi-P-rGO@Se cathode displayed exceptional electrochemical performance, such as excellent rate capabilities and overwhelming extended stable cycling performance. The superior electrochemical properties can be attributed to the high active material utilization and excellent conductivity of the Bi-P-rGO NFs as hosts. Therefore, we believe that the synthesis approach presented in this work will add substantial knowledge to the current understanding of the development of advanced porous and conductive nanostructures for various energy storage applications.

Experimental section

Sample prepartion

For electrospinning solution, 0.5 g of GO nanosheets were dispersed in 10 mL of ethanol by ultrasonication for 3 h until a homogeneous suspension was obtained. Afterward, 2.0 g of polyvinyl alcohol (PVA 2000, Kanto Chemical Co.) and 1.5 g of PS nanobeads (ϕ = 100 nm) were subsequently added to the above suspension with vigorous stirring overnight. Size-controlled PS nanobeads were synthesized using a previously reported emulsion-free polymerization technique [42,43]. The GO nanosheets were prepared from graphite flakes *via* the modified Hummers method [44]. The spinning solution was then loaded into a plastic syringe pump (12 mL) fitted with a 25-gauge stainless-steel needle and was ejected at a speed of 1.0 mL h^{-1}. The as-spun fibers were collected onto a rotating drum (180 rpm) covered with Al foil, which was set at a distance of 15 cm from the tip of the needle. The voltage applied between the collector and needle was fixed at 20 kV. The as-spun composite fibers were then stabilized at 200 °C for 12 h in air and subsequently carbonized at 600 °C for 3 h at a heating rate of 5 °C min^{-1} under a N_2 atmosphere. The fibers were then mixed with potassium hydroxide (KOH, Samchun Co.) in a 1:2 ratio using a mortar and pestle. The mixture was subsequently activated by heat treatment at 800 °C for 3 h at a ramp rate of 5 °C min^{-1} in a N_2 atmosphere. Thereafter, the fibers were subjected to an etching process using H_2O/HCl (1:1 vol %) for 24 h, washed several times with distilled water, and subsequently dried. The obtained etched fibers were then mixed with elemental Se powder (99.99 %, Sigma-Aldrich) in a mass ratio of 3:7 and subjected to two-stage heat treatment at 260 °C for 12 h followed by 350 °C for 1 h at a heating rate of 5 °C min^{-1} in N_2 atmosphere. The product is hereafter referred to as "Bi-P-rGO@Se NFs" where Bi-P stands for bimodal porous. For comparison, a unimodal porous sample with only meso-pores abbreviated as "P-rGO@Se NFs" was also synthesized using an identical process except without KOH activation.

Characterization techniques

The microstructures of the samples were observed using field-emission scanning electron microscopy (FE-SEM, Ultra Plus, Zeiss) and field-emission transmission electron microscopy (FE-TEM, JEM-2100F, JEOL, KBSI). The phases were investigated by X-ray diffraction (XRD, Bruker, D8 Discover) using Cu $K_{\alpha 1}$ radiation (1.5405 Å) at the Korea Basic Science Institute (Daegu). The structural properties of the Se-impregnated samples were measured using Raman spectroscopy (LabRam, HR800, Horiba Jobin-Yvon) at room temperature. The bonding environment of the prepared nanofibers was analyzed by X-ray photoelectron spectroscopy (XPS, K-Alpha, Thermo Scientific) with Al Kα radiation. The surface areas of the samples were measured using the Brunauer-Emmett-Teller (BET) technique with N_2 as the adsorbate gas. Thermogravimetric (TG) analysis was performed using a Pyris 1 TGA (Perkin Elmer) in the temperature range of 25–800 °C at a heating rate of 10 °C min^{-1} in a N_2 atmosphere.

Electrochemical measurements

The electrochemical performance of the samples was measured using a 2032-type coin cell assembly. The electrodes were prepared by mixing 70 wt% active materials, 20 wt% carbon black (Super-P) as a conductive agent, and 10 wt% sodium carboxymethyl cellulose (CMC) as a binder in deionized water, followed by coating onto Al foil using a doctor blade. The coated slurry was dried overnight at 60 °C in a hot air oven. Afterward, circular electrodes (ϕ = 14 mm) with an active material loading of $\sim$ 0.3 mg cm^{-2} were subsequently punched and transferred inside the glove box. Li metal and a microporous polypropylene film were used as the counter electrode and separator, respectively. The electrolyte was prepared by dissolving 1 M $LiPF_6$ in a 1:1 (v/v) mixture of ethylene carbonate and diethyl carbonate (EC/DEC). The coin cell assembly was performed inside a glove

box filled with high-purity Ar gas. Cyclic voltammetry (CV) measurements were performed at different scan rates in the range of 0.05–1.0 mV s^{-1}. The rate capability results were obtained at various current densities ranging from 0.5–20.0C (1C = 675 mA h g^{-1}) at ambient temperature. The voltage range for the CV and charge–discharge tests was set at 1.0–3.0 V throughout the experiments. All electrochemical tests were performed using a WBCS3000 battery cycler (WonATech). Electrochemical impedance spectroscopy (EIS) was conducted in the frequency range of 100 kHz to 10 mHz using a voltage perturbation of 10 mV.

Results and discussion

The synthesis mechanism of highly porous and conductive 1D nanofibers comprising rGO as a self-supporting matrix, along with bimodal pores i.e., meso-/ micropores, and uniformly filled chain-like Se (i.e., Bi-P-rGO@Se) is represented in Scheme 1. The as-spun fibers comprised GO nanosheets and size-controlled PS nanobeads (ϕ = 100 nm) homogeneously mixed in the PVA polymer (Scheme 1-①). During the carbonization process at 600 °C, the carbonaceous matrix formed *via* PVA-derived carbon (PVA-derived C), whereas the PS nanobeads decompose completely into gaseous products to form interconnected chain-like mesopores with a mean size of 42 nm (Scheme 1-②). The presence of mesopores not only facilitates effective electrolyte penetration, but also increases the active surface area in contact with the electrolyte. In addition, the GO nanosheets transform into a highly conductive rGO matrix that acts as a self-supporting skeleton to enhance the structural integrity of the nanofibers. The obtained nanofibers were then subjected to the chemical activation process using KOH *via* a second-stage heat treatment process at 800 °C, followed by repeated washing using H_2O/HCl (1:1 vol %) (Scheme 1-③). This process guarantees the formation of micropores into the PVA-derived C alongside mesopores, which subsequently aids in high-active-material impregnation. Finally, the Bi-P-rGO@Se NFs were obtained *via* a typical melt-diffusion process in which elemental Se was mixed with Bi-P-rGO NF and consequently heat-treated to fill the micropores with Se (Scheme 1-④). It is envisaged that in the absence of micropores, Se accumulates as bulky deposits over the mesopores, as shown in Scheme S1. The presence of bulky Se hinders the high active material utilization besides insufficient electrolyte infiltration. Therefore, the synergetic effects of the structural merits of Bi-P-rGO envisage superior electrochemical performance.

To explore the formation mechanism of the Bi-P-rGO@Se NF, morphological and phase analyses at each synthesis step were thoroughly investigated. The as-spun PVA/GO/PS composite fibers stabilized overnight at 200 ℃ are shown in Fig. S1. The fibers exhibited a continuous 1D fibrous morphology with an average diameter of *ca.* 500 nm (Fig. S1a). The cross-sectional FE-SEM image shown in Fig. S1b suggests that the GO nanosheets are well confined inside the fibrous framework. This is due to the dipole–dipole interaction of the carboxylic groups of GO with both PS nanobeads and PVA, resulting in a homogeneous distribution of GO nanosheets, PVA, and PS nanobeads in the spinning solution [45]. The XRD pattern in Fig. S1c exhibits a broad peak at approximately 2θ = 20° indicating the amorphous nature of the composite fibers. In addition, Raman spectra (Fig. S1d) was obtained to analyze the structural properties of the stabilized composite fibers. The spectrum exhibits broad peaks for the D-band and G-band, which are generally observed in the GO phase [45].

The unimodal porous rGO nanofibers (abbreviated as "P-rGO NFs") were initially obtained from the stabilized composite fibers at 600 °C in a N_2 atmosphere for 3 h, as shown in Fig. 1a–g. The FE-SEM image in Fig. 1a indicates fibrous morphology with a mean diameter of 400 nm. In addition, the fibers comprised well-formed mesopores all over the structure, as shown in the inset of Fig. 1a. The TEM image in Fig. 1b confirms the FE-SEM results and validates the presence of highly interconnected chain-like mesopores (ϕ = 42 nm) that are uniformly formed in the fibrous structure owing to the decomposition of PS nanobeads during carbonization. The HR-TEM image in Fig. 1c, along with the selected-area electron diffraction (SAED) pattern (Fig. S2a) confirms the existence of graphitic carbon in the fibers, which constitutes the rGO matrix, as evident from the diffraction rings corresponding to the (002), (100), and (110) crystal planes. During the heat treatment process, the GO nanosheets were converted to an rGO matrix. The well-formed rGO matrix acts as a self-supporting skeleton that increases the structural integrity of the nanofibers. Furthermore, the XRD pattern in Fig. 1d displays a broad peak centered at 2θ = 24° which corresponds to the carbonaceous products in the nanofibers [16]. The carbon content in the nanofibers originates from the PVA polymer after carbonization and the rGO nanosheets. The N_2 adsorption–desorption isotherm of the P-rGO NF in Fig. 1e exhibits type IV behavior, which indicates the presence of mesopores owing to the decomposition of PS nanobeads during the carbonization step. The presence of mesopores resulted in a BET surface area of 344 m^2 g^{-1} (pore volume: 0.59 cm^3 g^{-1}). Mesopores in the nanofibers (mean pore size of 42 nm) were also confirmed in the Barrett-

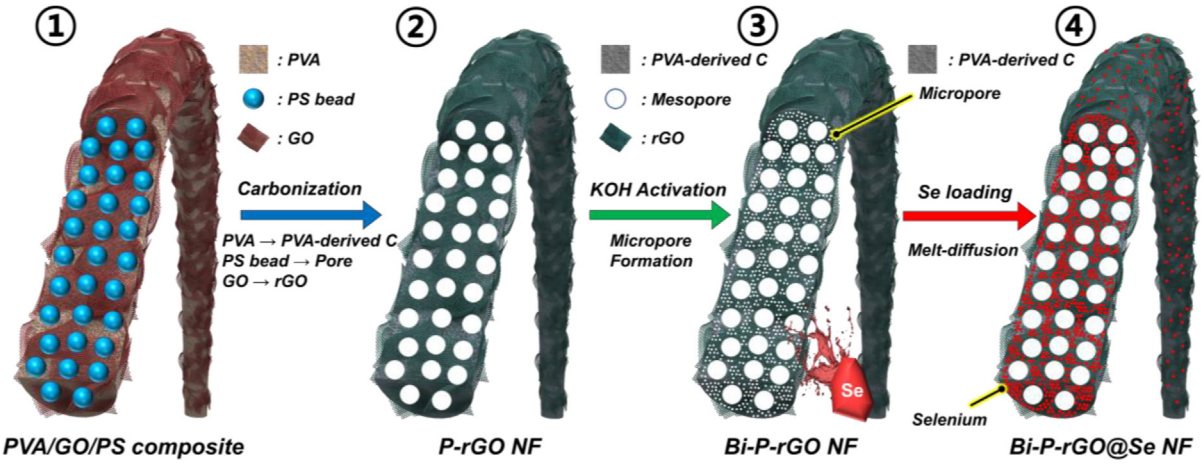

Scheme 1. Schematic representation of 1D reduced graphene oxide (rGO) nanofibers comprising bimodal pores and uniformly filled chain-like selenium as a high-performance cathode for stable lithium-selenium batteries.

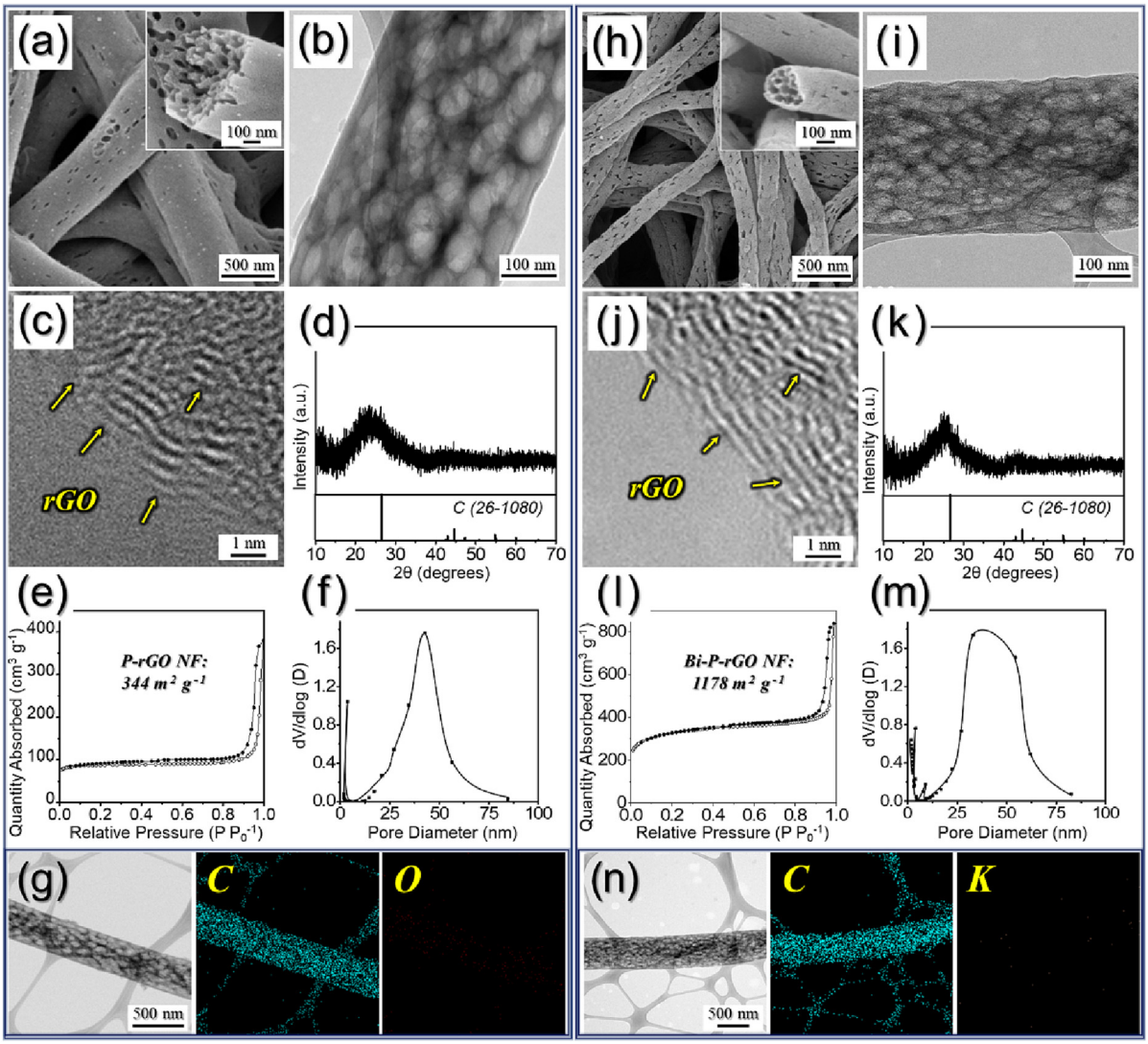

Fig. 1. Physical characterization results of (a-g) P-rGO and (h-n) Bi-P-rGO NFs: (a, h) FE-SEM micrographs and in inset is high-magnification FE-SEM images, (b, i) TEM images, (c, j) HR-TEM images, (d, k) XRD patterns, (e, i) N_2 adsorption–desorption isotherms, (f, m) BJH pore-size distribution curves, and (g, n) elemental dot mapping images.

Joyner-Halenda (BJH) pore size distribution curve (Fig. 1f). Additionally, the sharp peak at 3.8 nm is due to the tensile strength effect of N_2 desorption [46]. The elemental-mapping images shown in Fig. 1g suggest uniform dispersion of C only throughout the fiber length with no other element detected, indicating the carbonaceous structure of the fibers, confirming the XRD results in Fig. 1d.

The bimodal porous rGO nanofibers ("Bi-P-rGO NFs") were obtained from P-rGO NFs *via* a chemical activation process using KOH followed by heat treatment at 800 °C for 3 h in N_2 atmosphere, as shown in Fig. 1h–n. The FE-SEM micrographs in Fig. 1h suggest that the fibrous morphology remains intact even after the activation process, with a mean diameter of ~ 300 nm. The decrease in the fiber diameter was due to thermal contraction at a high temperature of 800 °C. In addition, the mesopores in the fibrous structure are also evident from the high-magnification FE-SEM image in the inset of Fig. 1h. The TEM image shown in Fig. 1i unambiguously validates the FE-SEM results. The presence of graphitic carbon due to the rGO matrix is also apparent in the HR-TEM image (Fig. 1j) and the SAED pattern (Fig. S2b). The XRD pattern in Fig. 1k exhibits a broad peak at $2\theta = 25°$, indicating the carbonaceous nature of the prepared nanofibers even after KOH activation. To confirm the existence of micropores generated by KOH activation, the N_2 adsorption–desorption isotherm (Fig. 1l) and BJH pore size distributions (Fig. 1m) were observed. The N_2 adsorption–desorption curve in Fig. 1l displays type I isotherm characteristics, implying the presence of micropores in the nanofibers. During the KOH activation process, potassium was inserted into the carbon matrix and subsequently etched to form micropores. The coexistence of meso-/micro pores resulted in a significant increase in the BET surface area of 1178 $m^2\ g^{-1}$ and pore volume of 1.30 $cm^3\ g^{-1}$ compared to the P-rGO NFs (BET surface area: 344 $m^2\ g^{-1}$, pore volume: 0.59 $cm^3\ g^{-1}$). The BJH pore size distribution curve in Fig. 1m indicates a sharp peak below 3 nm and a broad peak at 40 nm, thus confirming the presence of both meso- and micropores in the nanofibers. The elemental dot mapping images shown in Fig. 1n again confirm that the carbon is evenly distributed in the porous nanofiber, and no impurity species such as K have been detected, confirming the complete removal of the same during the etching and washing processes.

The elemental-Se-impregnated Bi-P-rGO (i.e., Bi-P-rGO@Se) and P-rGO (i.e., P-rGO@Se) NFs were obtained using the melt-diffusion process (both samples were mixed in a mass ratio of 3:7 with elemental Se and subsequently heat-treated for infiltration of Se). The physical characteristics of the Se-loaded resulting nanofibers are

shown in Fig. 2. The FE-SEM image of the P-rGO@Se NF in Fig. 2a confirms the fibrous morphology. In addition, the presence of bulky Se deposits over the mesopores is also evident (inset images of Fig. 2a and (b)). The incomplete impregnation of Se was primarily due to the absence of micropores in the nanofibers. The TEM images in Fig. 2b firmly validate the FE-SEM results with the clear presence of bulky Se nanoparticles (ϕ = 60 nm) that agglomerate during the melt diffusion process over the mesopores of the P-rGO NFs (inset image). The HR-TEM images in Fig. 2c reveal clear lattice fringes corresponding to the (100) planes of elemental-Se and the (002) planes of rGO separated by 0.38 and 0.34 nm, respectively [35]. The SAED pattern in Fig. 2d also displays the diffraction planes corresponding to single-crystalline Se nanoparticles. Additionally, the sharp crystalline peaks in the XRD pattern (Fig. 2e) firmly suggest the presence of elemental Se as a separate entity deposited over the mesopores. The N_2 adsorption–desorption isotherms (Fig. 2f) and Barrett-Joyner-Halenda (BJH) pore size distribution curve (Fig. S3a) of the P-rGO@Se NF clearly indicate that the deposition of bulky Se over the mesopores significantly decreases the BET surface area (18 m^2 g^{-1}, pore volume: 0.10 cm^3 g^{-1}). The elemental-mapping images in Fig. 2g also validate that Se nanoparticles are present all over the fiber surface with minimum impregnation.

The physical characterizations of the Bi-P-rGO@Se NFs obtained after the melt-diffusion process are shown in Fig. 2h–n. The FE-SEM image in Fig. 2h, along with the inset image, confirms that the porous 1D fibrous structure is well maintained even after Se impregnation. Likewise, the TEM image in Fig. 2i also indicates chain-like interconnected mesopores (bright region) within the carbon framework (grey region). Additionally, unlike the P-rGO@Se NFs, no bulky elemental Se nanoparticles were observed (Fig. 2i), indicating that the nano-sized Se infiltrated well into the micropores (<3 nm; formed *via* KOH activation) during melt diffusion without agglomeration. The HR-TEM images in Fig. 2j revealed graphitic carbon only primarily due to the rGO matrix. Moreover, the SAED and XRD patterns in Fig. 2(k, l) further indicate the presence of a carbonaceous phase, implying that the nanosized Se has infiltrated well inside the porous carbon skeleton. The N_2 isotherms and BJH pore size distributions in Fig. 2m and Fig. S3b, respectively, also confirm the filling of pores with nanosized Se, as evident from the sharp decrease in the BET surface area (67 m^2 g^{-1}, pore volume: 0.14 cm^3 g^{-1}). Furthermore, the elemen-

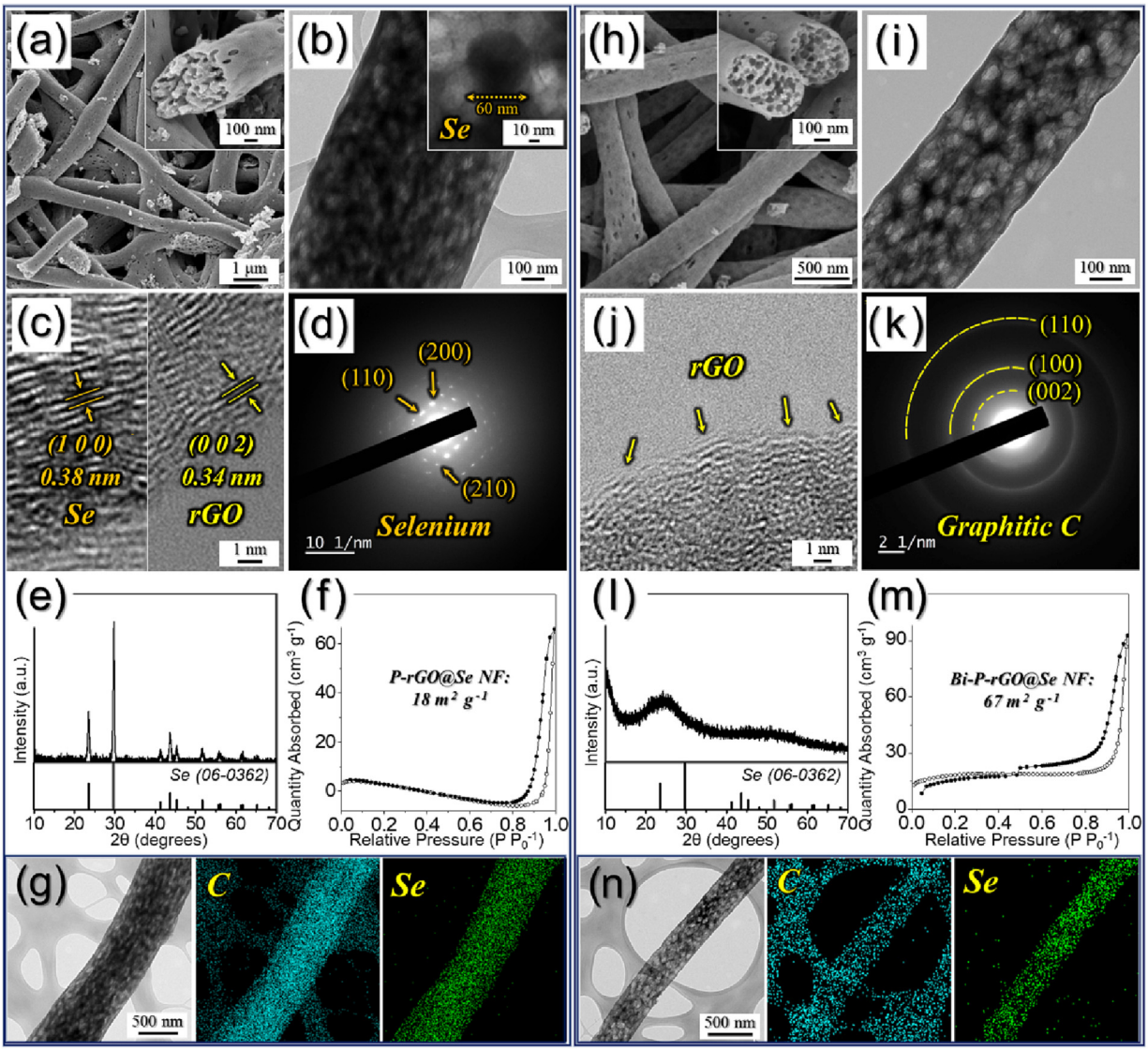

Fig. 2. Physical characterization results of (a-g) P-rGO@Se and (h-n) Bi-P-rGO@Se NFs: (a, h) FE-SEM micrographs and in inset is high-magnification FE-SEM images, (b, i) TEM images, (c, j) HR-TEM images, (d, k) SAED patterns, (e, i) XRD patterns, (f, m) N_2 adsorption–desorption isotherms, and (g, n) elemental dot mapping images.

tal dot mapping images in Fig. 2n indicate that Se is uniformly distributed within the porous nanofiber. Overall, the FE-SEM, TEM, XRD, and BET results of the Bi-P-rGO@Se NFs validate that nanosized Se is successfully impregnated inside the porous nanostructure compared to the P-rGO@Se NFs.

The chemical states and molecular environments of various elements in the Bi-P-rGO@Se NF were characterized *via* X-ray photoelectron spectroscopy (XPS) analysis, as shown in Fig. 3a–c. The survey spectrum in Fig. 3a shows photoelectron signals corresponding to the C 1 s, Se 3p, and Se 3d orbitals. The high-resolution C 1 s XPS spectrum in Fig. 3b displays three well-fitted peaks corresponding to the sp^2-hybridized C═C (284.7 eV), sp^3-hybridized C—C (285.1 eV), and C═O (287.5 eV) species [16,26,46–49]. The highly intense sp^2-hybridized C═C peak confirmed the existence of carbonaceous products in the nanofibers, which were present in the form of graphitic carbon from the rGO matrix. The deconvoluted Se 3d spectrum in Fig. 3c exhibits two major peaks attributed to the Se $3d_{5/2}$ (55.9 eV) and Se $3d_{3/2}$ (56.7 eV) states, confirming the presence of infiltrated Se [27,50]. The Se content in the nanofibers was quantified using TG analysis (Fig. 3d). As observed, the Bi-P-rGO@Se and P-rGO@Se NFs contain almost 50.7 and 43.3 wt% of elemental Se, respectively. The higher Se amount for the Bi-P-rGO@Se NFs again suggests that a high micropore volume is available during the impregnation process. Besides, sharp weight loss at a higher temperature of 375 °C was observed for Bi-P-rGO@Se compared to P-rGO@Se (~343 °C). This is due to relatively strong chemical interaction between the chain-like Se (i.e., c-Se) and carbonaceous species in Bi-P-rGO@Se. Furthermore, the structural characteristics of Bi-P-rGO@Se and P-rGO@Se NFs were investigated *via* Raman spectroscopy, as shown in Fig. 3(e, f). The high-wavenumber Raman spectra in Fig. 3e indicate the presence of D-(1360 cm^{-1}) and G-

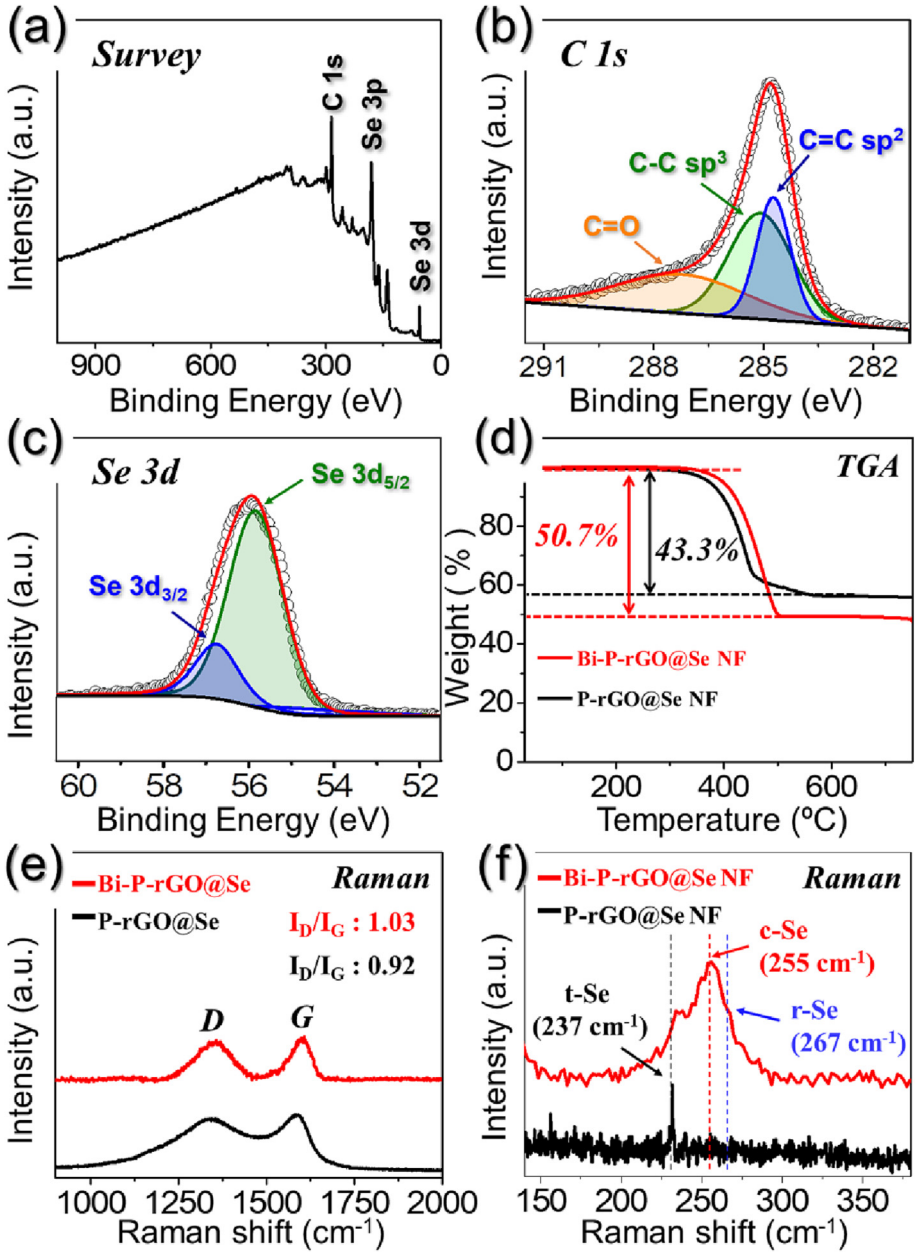

Fig. 3. (a) XPS survey spectrum, (b) core level C 1 s XPS and (c) core level Se 3d XPS for Bi-P-rGO@Se NFs, (d) TG curves of Bi-P-rGO@Se and P-rGO@Se NFs for elemental-Se quantification, (e) high-wavenumber side and (f) low-wavenumber side Raman spectra of Bi-P-rGO@Se and P-rGO@Se.

bands (1600 cm^{-1}) for both samples. The G-band originates from the presence of sp^2-hybridized carbon species in rGO, whereas the D-band corresponds to disordered AC formed by the decomposition of PVA. Furthermore, the degree of crystallinity of the carbonaceous products was determined using the relative intensity ratio of the two bands i.e., I_D/IG [51]. The I_D/IG ratio was observed to be 1.03 for Bi-P-rGO@Se and 0.92 for P-rGO@Se NFs, respectively, indicating the presence of more defects in Bi-P-rGO@Se that may arise because of the chemical activation process using KOH. Furthermore, the low-wavenumber Raman spectrum for Bi-P-rGO@Se NFs in Fig. 3f exhibits three peaks corresponding to trigonal (t-Se, 237 cm^{-1}), chain (c-Se, 255 cm^{-1}), and ring- (r-Se, 267 cm^{-1})-type Se [26]. In contrast, the P-rGO@Se NFs only exhibit a high-intensity band centered at 237 cm^{-1} corresponding to t-Se attributed to the bulky Se filled in the mesopores as described in Scheme S1. The highest peak intensity for c-Se at 255 cm^{-1} mainly arises from the presence of micropores that favor short-range ordering in Bi-P-rGO@Se. Therefore, the Raman results suggest that the presence of c-Se in Bi-P-rGO@Se offers high Se utilization and thus provides superior electrochemical performance compared to the P-rGO@Se.

To authenticate the structural advantages of the Bi-P-rGO@Se NFs, electrochemical performance was evaluated using a CR2032 coin cell. The assembled cells were initially subjected to CV tests at 0.1 mV s^{-1} in the voltage range of 1.0–3.0 V for five initial cycles. The first CV scan in Fig. 4a for Bi-P-rGO@Se NFs displays the low-intensity peak at 2.31 V (marked as 'red arrow') that corresponds to the transformation of r-Se to c-Se [52]. However, the complete transformation during the first cycle results in the disappearance of the peak at 2.31 V during the subsequent reduction cycles. Furthermore, the sharp reduction peak located at 1.76 V is attributed to the formation of Li_2Se from c-Se, which is consistent with previous reports [53]. During the anodic scan, a single peak is observed at 2.06 V corresponding to the conversion of Li_2Se back to Se, thus completing the 2Li + Se ↔ Li_2Se redox cycle [28]. It should be noted that the conversion reaction is a solid–solid process owing to the insolubility of lithium polyselenides in carbonate-based electrolytes. In addition, the anodic peak remains stable during subsequent cycles (Fig. S4a). However, the CV curves of P-rGO@Se (Fig. 4a and Fig. S4b) display slightly different characteristics compared to those of Bi-P-rGO@Se. For instance, the irreversible peaks observed at 2.35 and 2.20 V (marked as 'blue arrow') correspond to the r-Se to c-Se transformation and disappear during subsequent reduction cycles, as shown in Fig. S4b. Moreover, two oxidation peaks at 1.9 and 2.3 V are observed during the charging process, which are attributed to the stepwise conversion of Li_2Se to lithium polyselenides, and then to elemental Se, respectively [21,52,54]. Moreover, a noticeable difference in the shape and intensity of the redox peaks is evident, implying poor redox reaction kinetics inside the cell. This observation is more prominent when the polarization potential (ΔV) of the prepared nanofibers is considered. For instance, the cell employing the Bi-P-rGO@Se cathode displays a lower separation between redox peaks (i.e., ΔV = 300 mV) compared to the P-rGO@Se cathode (ΔV = 390 mV). Furthermore, after the first cycle onwards, the reduction peaks in both samples (Fig. S4a, b) shift considerably towards a higher potential, primarily owing to the deformation of the cathode during the lithiation process [55]. In addition, the smaller of the voltage shift in Bi-P-rGO@Se compared to that in P-rGO@Se indicates superior electrochemical activity in the Bi-P-rGO@Se sample. Furthermore, a new shoulder peak at 1.7 V (marked as '*' in Fig. S4a) appears in the cathodic scan after 2nd cycle for Bi-P-rGO@Se sample corresponding to the reaction of lithium with two different Se molecules possessing different chain length [56]. Subsequently, the well-overlapped and symmetric CV curves indicate highly reversible redox processes. In addition, the CV curves for the Bi-P-rGO@Se cathode display higher current densities than those of P-rGO@Se, which clearly signify enhanced redox reaction kinetics inside the cell compared to the P-rGO@Se cathode.

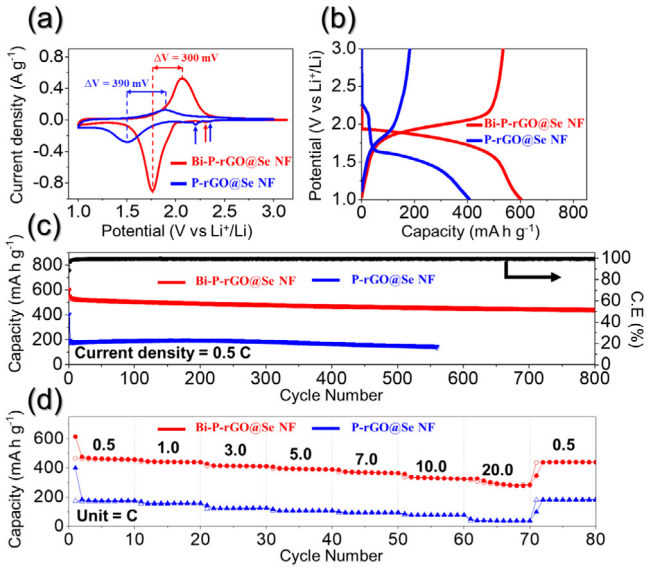

Fig. 4. Electrochemical performance of Bi-P-rGO@Se and P-rGO@Se NFs: (a) first CV scans at 0.1 mV s^{-1}, (b) initial charge–discharge profiles at 0.5C-rate, (c) cycling performance at 0.5C-rate, and (d) rate capability test at various C-rates.

The CV curves were further verified using the charge–discharge profiles obtained at a C-rate of 0.5, as shown in Fig. 4b. The charge–discharge profiles display voltage plateaus that are consistent with the CV curves. For instance, the Bi-P-rGO@Se cathode displays a long discharge voltage plateau at approximately 1.9 V corresponding to the conversion of elemental Se to Li_2Se [26]. Similarly, the charge plateau at 1.95 V corresponds to the transformation of Li_2-Se to Se [28]. In contrast, the P-rGO@Se cathode displays short charge–discharge voltage plateaus at 1.81 (Li_2Se → Se) and 1.60 V (Se → Li_2Se), implying that the discharge capacity values are lower than those of the Bi-P-rGO@Se cathode. In addition, the sloppy discharge plateau of the P-rGO@Se cathode at approximately 2.25 V is due to the transformation from r-Se to c-Se [52]. The Bi-P-rGO@Se and P-rGO@Se cathodes exhibit initial discharge capacities of 603 and 408 mA h g^{-1}, respectively. In addition, a high Coulombic efficiency of 86 % is observed for Bi-P-rGO@Se compared with 47 % for the P-rGO@Se cathode. The high initial capacity loss or poor initial Coulombic efficiency of the P-rGO@Se cathode is ascribed to the presence of bulky Se, which subsequently dissolves to form lithium polyselenide. However, Bi-P-rGO@Se loaded with chain-like Se in the micropores mitigates polyselenide dissolution, limiting the multistep reaction between Li and Se into a single-step reaction. The high discharge capacity of the Bi-P-rGO@Se cathode can be attributed to the high utilization of chain-like Se as an active material in the micropores. In contrast, the low discharge capacity of the P-rGO@Se cathode can be attributed to the presence of bulky Se deposits that remain unutilized during the redox process, as evidenced by the short charge–discharge plateau [28]. Overall, the CV and initial charge–discharge profiles prove that the synergetic effects of the highly porous and conductive skeleton in the Bi-P-rGO@Se cathode results in enhanced electrochemical performance.

The cycling performance was further analyzed to validate the structural advantages of the as-prepared Bi-P-rGO@Se NFs (Fig. 4c). The cycling performance at 0.5C-rate indicates that the Bi-P-rGO@Se cathode exhibits an initial discharge capacity of

603 mA h g^{-1} compared to 408 mA h g^{-1} for P-rGO@Se. As the cycling proceeds, the Bi-P-rGO@Se cathode exhibits a discharge capacity of 441 mA h g^{-1} (73 % capacity retention) at the end of 800th continuous charge–discharge cycles. In contrast, the P-rGO@Se display low-capacity values throughout the cycling, although stable. The P-rGO@Se exhibited a discharge capacity of 149 mA h g^{-1} after 560th cycles (37 % capacity retention). Additionally, a low average capacity decay of 0.03 % per cycle for the Bi-P-rGO@Se cathode compared to 0.11 % for P-rGO@Se further validates the structural advantages of the former. The high Coulombic efficiency of 99 % throughout the cycling process also explains the high reversibility of the redox processes inside the cell. These results are more obvious when considering the charge–discharge profiles at various cycle numbers (Fig. S4c, d). As observed, the high discharge capacities of the Bi-P-rGO@Se cathode are primarily due to the well-formed long voltage plateaus (Fig. S4c) compared to the P-rGO@Se cathode (Fig. S4d). The cycling results again validate the high active material utilization in Bi-P-rGO@Se compared to P-rGO@Se, where the low capacity clearly signifies a high proportion of unutilized active material (bulky Se deposits), which subsequently results in slow reaction kinetics inside the cells.

The rate was also obtained for the as-prepared nanofibers to gain more insight into their electrochemical performance, as shown in Fig. 4d. The Bi-P-rGO@Se cathode exhibits discharge capacities of 613, 454, 428, 407, 385, 357, and 326 mA h g^{-1} at C-rates of 0.5, 1.0, 3.0, 5.0, 7.0, 10.0, and 20.0, respectively. Moreover, when the current is reversed to 0.5C, the cathode displays a stable discharge capacity of 440 mA h g^{-1}. In contrast, the P-rGO@Se cathode exhibits low discharge capacities of 400, 169, 143, 117, 101, 85, and 50 mA h g^{-1} at the identical C-rates as mentioned above. The Bi-P-rGO@Se cathode exhibits high discharge capacities even at a high C-rate of 20.0C. The excellent cycling stability and overwhelming rate capability of the Bi-P-rGO@Se cathode can be attributed to the 1D bimodal porous structure containing mesopores and micropores, which guarantees high active material utilization in addition to efficient electrolyte percolation or wetting of the electrode. Additionally, the highly conductive rGO matrix not only increases the structural integrity of the electrode but also provides numerous conductive channels that support fast charge-transfer redox kinetics.

To authenticate the superior redox kinetics inside the Li–Se cell employing Bi-P-rGO@Se cathode, the Li–ion diffusion coefficient (D_{Li}^{+}) was calculated by examining the CV data in a voltage range of 1.0–3.0 V and at different scan rates from 0.05–1.0 mV s^{-1}, as shown in Fig. 5. The CV curves obtained at various voltage scan rates exhibit typical Li–Se redox peaks, suggesting that the electrochemical processes inside the cells occurred between elemental Se and Li_2Se *via* a solid–solid process. The high current intensity values were observed for the Bi-P-rGO@Se cathode (Fig. 5a) even at a high voltage scan rate of 1.0 mV s^{-1} compared to the P-rGO@Se cathode (Fig. 5c), implying fast electrochemical processes inside the cell. The Randles–Sevcik equation was further applied to measure the D_{Li}^{+} values for all the cells and shown in Equation (1) [57]:

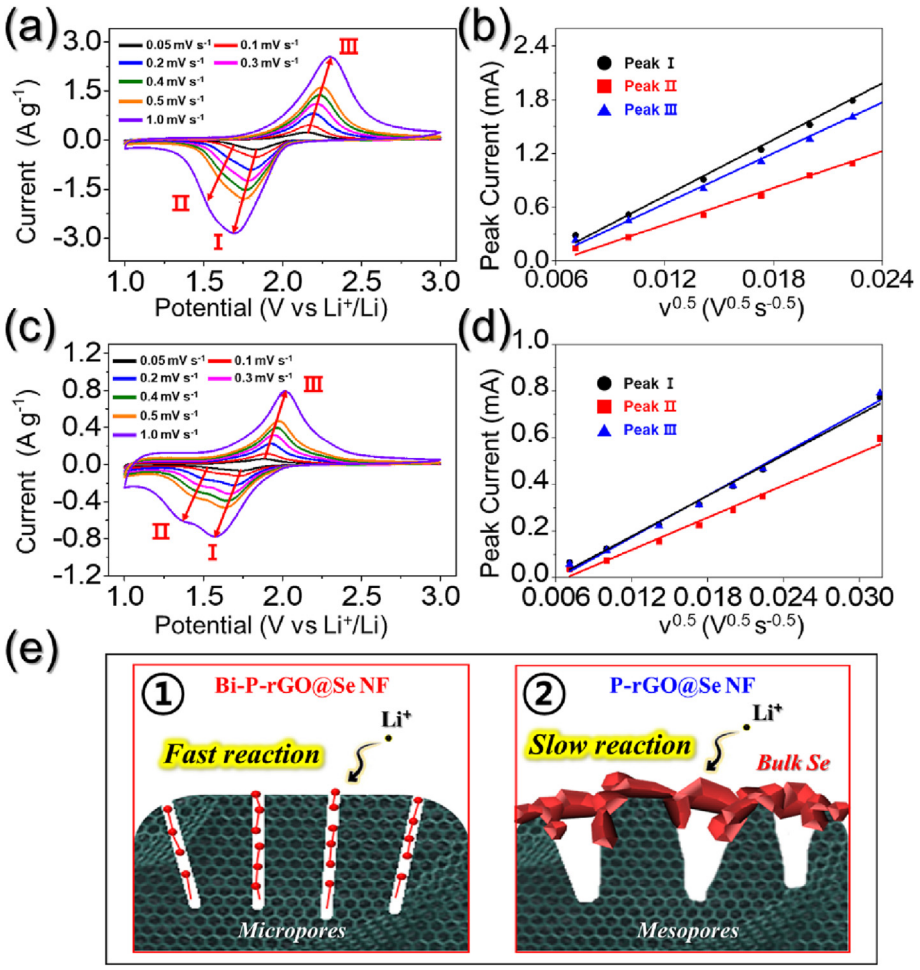

Fig. 5. Lithium–ion diffusion coefficient (D_{Li}^{+}) for the assembled Li–Se cells with different cathodes: (a, b) Bi-P-rGO@Se, (c, d) P-rGO@Se, and schematic illustrations of (e-①) Se-impregnated into micropores of Bi-P-rGO@Se cathode and (e-②) into mesopores of P-rGO@Se cathode.

$$I_p = 2.69 \times 10^5 n^{1.5} A D_{Li^+}^{0.5} C_{Li} v^{0.5} \quad (1)$$

where I_p represents the redox peak current, n is the number of electrons involved in the redox reaction (n = 2), A is the electrode surface area (cm^2), C_{Li} is the Li–ion concentration (mol L^{-1}), and v is the voltage scan rate (V s^{-1}). The I_p vs $v^{0.5}$ plots obtained for the Bi-P-rGO@Se and P-rGO@Se cathodes are shown in Fig. 5(b, d), and the D_{Li}^{+} values calculated for all Li–Se cells are presented in Table S1. As observed, the Li–Se cell employing Bi-P-rGO@Se cathode exhibited one order higher Li-ion diffusion coefficient value (5.99×10^{-9} cm^2 s^{-1}) compared to the P-rGO@Se cathode (0.55×10^{-9} cm^2 s^{-1}), indicating superior diffusion kinetics inside the cell. The high diffusion coefficient results again confirm that the unique 1D design strategy accompanied by chain-like Se filled in micropores results in kinetically favored redox kinetics, which in turn enhances the overall improvement in the electrochemical performance (Fig. 5e-①). In contrast, the high proportion of unutilized active material (bulky Se deposits) in the P-rGO@Se cathode results in slow reaction kinetics inside the cells, leading to poor electrochemical properties (Fig. 5e-②).

The improved reaction kinetics inside the assembled Li–Se cell utilizing the Bi-P-rGO@Se cathode were further confirmed *via* EIS, as shown in Fig. 6. The equivalent circuit model consisting of all fitted impedance parameters is presented in Fig. S5. The impedance of all Li–Se cells was measured in a fresh or uncycled state, as well as at different cycle numbers in a fully charged state during cycling at 0.5C. The Li–Se cells employing the Bi-P-rGO@Se cathode display the lowest charge-transfer resistance (R_{ct}) throughout the cycling process compared to the P-rGO@Se cathode. For instance, the fresh cell utilizing the Bi-P-rGO@Se cathode display an R_{ct} value of 172 Ω (Fig. 6a), which decreases sharply to 54 Ω (Fig. 6b) after the first cycle and remains mostly stable even after the 100th cycle. In contrast, the Li–Se cell employing the P-rGO@Se cathode (Fig. 6a and c) displays higher R_{ct} values (75 Ω after the 100th cycle) than Bi-P-rGO@Se. These results again verify that the structural advantages of Bi-P-rGO@Se not only guarantee a kinetically favored redox process inside the Li–Se cell but also enhance the structural integrity of the Se electrode during prolonged cycling. The FE-SEM micrograph of the Bi-P-rGO@Se (Fig. 6d) and P-rGO@Se (Fig. S6) cathodes obtained after the 100th cycle at 0.5C firmly validate the above arguments. The 1D fibrous morphology of the Bi-P-rGO@Se cathode remained intact compared to P-rGO@Se, thus explaining the excellent structural robustness of the prepared cathode. The structural advantages in Bi-P-rGO@Se cathode not only allows higher active material impregnation but also accommodates large volume variations along with the efficient lithium polyselenide anchoring during the electrochemical processes. The digital images of the glass fiber surface faced towards the lithium anode and paired with different cathodes were further analyzed for polyselenide anchoring, as shown in Fig. S7. The white color of glass fiber paired with Bi-P-rGO@Se cathode (Fig. S7a) compared to the dark color of glass fiber utilized with P-rGO@Se cathode (Fig. S7b) firmly indicates better capturing and reutilization of polyselenide species.

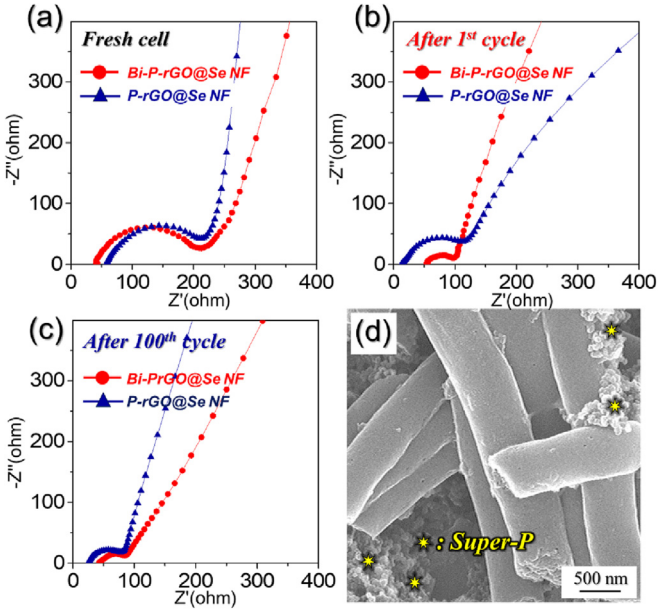

Fig. 6. Nyquist plots of Bi-P-rGO@Se and P-rGO@Se cathode: (a) fresh cells, (b) after 1st cycle, (c) after 100th cycles at 0.5C-rate, and (d) FE-SEM micrograph of Bi-P-rGO@Se cathode obtained after 100th cycle at 0.5C-rate.

Overall, the utilization of 1D nanofibers consisting of bimodal pores and a highly conductive rGO matrix (i.e., Bi-P-rGO) as an active material host to obtain a high-performance Bi-P-rGO@Se cathode demonstrated improved electrochemical performance, such as excellent rate capabilities and overwhelming prolonged cycling stabilities. Therefore, we believe that the facile synthesis strategy adopted in the present work will significantly improve the present understanding of the evolution of highly porous and conductive 1D nanostructures for various energy-storage applications.

Conclusion

In summary, we explored the electrochemical performance of Li–Se cells by synthesizing 1D reduced graphene oxide nanofibers composed of bimodal meso-/micropores (i.e., Bi-P-rGO NFs) as a cathode host using a conventional electrospinning technique. The highly conductive rGO not only provides numerous conducting pathways, but also serves as a self-supporting skeleton to enhance the structural integrity of the nanostructure. Similarly, the bimodal porous structure simultaneously provides highly interconnected chain-like mesopores and KOH-derived micropores for efficient electrolyte percolation and active material impregnation, respectively. Subsequently, Bi-P-rGO@Se as a high-performance cathode was visualized, which demonstrated an overall improved electrochemical performance, such as excellent rate capability (326 mA h g^{-1} at 20.0C) and overwhelming long-term cycling stability (441 mA h g^{-1} at the end of the 800th cycle with an average capacity decay rate of just 0.03 % per cycle at 0.5C-rate). The structural and electrochemical results presented in this work represent a step forward in the development of porous and conductive nanostructures for a wide range of applications.

Declaration of Competing Interest

The authors declare that they have no known competing financial interests or personal relationships that could have appeared to influence the work reported in this paper.

Acknowledgements

This work was supported by the National Research Foundation of Korea (NRF), funded by the Korean government (MSIP) [grant numbers NRF-2021R1A4A2001687, NRF-2021R1I1A3057700, and NRF-2021R1I1A1A01059490].

Appendix A. Supplementary data

Supplementary data to this article can be found online at https://doi.org/10.1016/j.jiec.2023.02.004.

References

[1] M. Rahman, X. Wang, C. Wen, J Appl Electrochem 44 (2014) 5–22, https://doi.org/10.1007/s10800-013-0620-8.
[2] R. Saroha, A.K. Panwar, Y. Sharma, P.K. Tyagi, S. Ghosh, Appl. Surf. Sci. 394 (2017) 25–36, https://doi.org/10.1016/j.apsusc.2016.09.105.
[3] A. Manthiram, A.C.S. Cent, Sci. 3 (2017) 1063–1069, https://doi.org/10.1021/acscentsci.7b00288.
[4] R. Saroha, A.K. Panwar, Y. Sharma, Ceram. Int. 43 (2017) 5734–5742, https://doi.org/10.1016/j.ceramint.2017.01.115.
[5] R. Saroha, A. Gupta, A.K. Panwar, J. Alloys Compd. 696 (2017) 580–589, https://doi.org/10.1016/j.jallcom.2016.11.199.
[6] J. Duan, X. Tang, H. Dai, Y. Yang, W. Wu, X. Wei, Y. Huang, Electrochem. Energ. Rev. 3 (2020) 1–42, https://doi.org/10.1007/s41918-019-00060-4.
[7] T. Chen, Y. Jin, H. Lv, A. Yang, M. Liu, B. Chen, Y. Xie, Q. Chen, Trans. Tianjin Univ 26 (2020) 208–217, https://doi.org/10.1007/s12209-020-00236-w.
[8] Y.H. Seon, R. Saroha, J.S. Cho, Compos. B. Eng. 237 (2022), https://doi.org/10.1016/j.cej.2022.137141.
[9] R. Saroha, J.H. Oh, Y.H. Seon, Y.C. Kang, J.S. Lee, J.S. Cho, J. Mater. Chem. A 9 (2021) 11651–11664, https://doi.org/10.1039/D1TA01802G.
[10] L. Zhou, H. Li, X. Wu, Y. Zhang, D.L. Danilov, R.A. Eichel, P.H. Notten, ACS Appl. Energy Mater. 2 (2019) 8153–8162, https://doi.org/10.1021/acsaem.9b01621.
[11] R. Saroha, J.-H. Ahn, J.S. Cho, Korean J. Chem. Eng. 38 (2021) 461–474, https://doi.org/10.1007/s11814-020-0729-5.
[12] R. Saroha, J. Heo, X. Li, N. Angulakshmi, Y. Lee, H.-J. Ahn, J.-H. Ahn, J.-H. Kim, J. Alloys Compd. 893 (2022), https://doi.org/10.1016/j.jallcom.2021.162272.
[13] J. He, A. Bhargav, H. Yaghoobnejad Asl, Y. Chen, A. Manthiram, Adv. Energy Mater. 10 (2020) 2001017, https://doi.org/10.1002/aenm.202001017.
[14] J.M. Choi, R. Saroha, J.S. Kim, M.R. Jang, J.S. Cho, J. Power Sources 559 (2023), https://doi.org/10.1016/j.jpowsour.2023.232632.
[15] R. Saroha, J. Heo, Y. Liu, N. Angulakshmi, Y. Lee, K.-K. Cho, H.-J. Ahn, J.-H. Ahn, Chem. Eng. J. 431 (2022), https://doi.org/10.1016/j.cej.2021.134205.
[16] R. Saroha, J.S. Cho, Small Methods 6 (2022) 2200049–2200064, https://doi.org/10.1002/smtd.202200049.
[17] M. Gao, W.-Y. Zhou, Y.-X. Mo, T. Sheng, Y. Deng, L. Chen, K. Wang, Y. Tan, H. Zhou, Advanced Powder Materials 1 (2022) 100006–100014, https://doi.org/10.1016/j.apmate.2021.09.006.
[18] R. Saroha, H.S. Ka, J.S. Cho, Appl. Surf. Sci. 612 (2023), https://doi.org/10.1016/j.apsusc.2022.155892.
[19] B. Yu, D. Chen, Z. Wang, F. Qi, X. Zhang, X. Wang, Y. Hu, B. Wang, W. Zhang, Y. Chen, Chem. Eng. J. 399 (2020), https://doi.org/10.1016/j.cej.2020.125837.
[20] A. Abouimrane, D. Dambournet, K.W. Chapman, P.J. Chupas, W. Weng, K. Amine, J. Am. Chem. Soc. 134 (2012) 4505–4508, https://doi.org/10.1021/ja211766q.
[21] J. He, Y. Chen, W. Lv, K. Wen, P. Li, Z. Wang, W. Zhang, W. Qin, W. He, ACS Energy Lett. 1 (2016) 16–20, https://doi.org/10.1021/acsenergylett.6b00015.
[22] A. Eftekhari, Sustain. Energy Fuels. 1 (2017) 14–29, https://doi.org/10.1039/C6SE00094K.
[23] Y. Liu, L. Si, Y. Du, X. Zhou, Z. Dai, J. Bao, J. Phys. Chem. C 119 (2015) 27316–27321, https://doi.org/10.1021/acs.jpcc.5b09553.
[24] J. He, W. Lv, Y. Chen, J. Xiong, K. Wen, C. Xu, W. Zhang, Y. Li, W. Qin, W. He, J. Power Sources 363 (2017) 103–109, https://doi.org/10.1016/j.powsour.2017.07.065.
[25] J.T. Lee, H. Kim, M. Oschatz, D.C. Lee, F. Wu, H.T. Lin, B. Zdyrko, W.I. Cho, S. Kaskel, G. Yushin, Adv. Energy Mater. 5 (2015) 1400981–1400987, https://doi.org/10.1002/aenm.201400981.
[26] S.-K. Park, J.-S. Park, Y.C. Kang, J. Mater. Chem. A 6 (2018) 1028–1036, https://doi.org/10.1039/C7TA09676C.
[27] Y. Liu, L. Si, X. Zhou, X. Liu, Y. Xu, J. Bao, Z. Dai, J. Mater. Chem. A 2 (2014) 17735–17739, https://doi.org/10.1039/C4TA03141E.
[28] Z. Lei, Y. Lei, X. Liang, L. Yang, J. Feng, J. Power Sources 473 (2020) 228611–228618, https://doi.org/10.1016/j.jpowsour.2020.228611.
[29] L. Fan, P. Sun, L. Yang, Z. Xu, J. Han, Korean J. Chem. Eng. 37 (2020) 166–175, https://doi.org/10.1007/s11814-019-0414-8.
[30] E. Lim, J. Chun, C. Jo, J. Hwang, Korean J. Chem. Eng. 38 (2021) 227–247, https://doi.org/10.1007/s11814-020-0693-0.
[31] Z. Zhang, X. Yang, Z. Guo, Y. Qu, J. Li, Y. Lai, J. Power Sources 279 (2015) 88–93, https://doi.org/10.1016/j.jpowsour.2015.01.001.
[32] H. Wang, S. Li, Z. Chen, H.K. Liu, Z. Guo, RSC Adv. 4 (2014) 61673–61678, https://doi.org/10.1039/C4RA10967H.
[33] W. Ye, K. Wang, W. Yin, W. Chai, Y. Rui, B. Tang, Dalton Trans. 48 (2019) 10191–10198, https://doi.org/10.1039/C9DT01961H.
[34] J. Li, X. Zhao, Z. Zhang, Y. Lai, J. Alloys Compd. 619 (2015) 794–799, https://doi.org/10.1016/j.jallcom.2014.09.099.
[35] Q. Xia, J. Hu, Q. Chen, L. Zhang, J. Colloid Interface Sci. 610 (2022) 643–652, https://doi.org/10.1016/j.jcis.2021.11.106.
[36] K. Han, Z. Liu, J. Shen, Y. Lin, F. Dai, H. Ye, Adv. Funct. Mater. 25 (2015) 455–463, https://doi.org/10.1002/adfm.201402815.
[37] Z.-P. Zhuang, X. Dai, W.-D. Dong, L.-Q. Jiang, L. Wang, C.-F. Li, J.-X. Yang, L. Wu, Z.-Y. Hu, J. Liu, L.-H. Chen, Y. Li, B.-L. Su, Electrochim. Acta 393 (2021) 139042. https://doi.org/10.1016/j.electacta.2021.139042.
[38] A.H.A. Hoseini, M.H.A. Shiraz, L. Tao, W. Lu, M. Arjmand, J. Liu, Electrochim. Acta 429 (2022), https://doi.org/10.1016/j.electacta.2022.140954.
[39] K. Balakumar, N. Kalaiselvi, Carbon 112 (2017) 79–90, https://doi.org/10.1016/j.carbon.2016.10.097.
[40] L. Zeng, W. Zeng, Y. Jiang, X. Wei, W. Li, C. Yang, Y. Zhu, Y. Yu, Adv. Energy Mater. 5 (2015) 1401377–1401386, https://doi.org/10.1002/aenm.201401377.
[41] J. Li, J. Song, L. Luo, H. Zhang, J. Feng, X. Zhao, X. Guo, H. Dong, S. Chen, H. Liu, Adv. Energy Mater. 12 (2022) 2200894, https://doi.org/10.1002/aenm.202200894.
[42] S.Y. Jeong, S.K. Park, Y.C. Kang, J.S. Cho, Chem. Eng. J. 351 (2018) 559–568, https://doi.org/10.1016/j.cej.2018.06.130.
[43] J.S. Lee, J.-S. Park, K.W. Baek, R. Saroha, S.H. Yang, Y.C. Kang, J.S. Cho, Chem. Eng. J. (2022), https://doi.org/10.1016/j.cej.2022.141118.
[44] G.D. Park, J.S. Cho, Y.C. Kang, ACS Appl. Mater. Interfaces 7 (2015) 16842–16849, https://doi.org/10.1021/acsami.5b04891.
[45] C.S. Kim, J.S. Lee, R. Saroha, Y.B. Park, Y.C. Kang, D.W. Kang, S.M. Jeong, J.S. Cho, J. Power Sources 523 (2022) 231030–231042, https://doi.org/10.1016/j.jpowsour.2022.231030.
[46] J.S. Lee, M.S. Jo, R. Saroha, D.S. Jung, Y.H. Seon, J.S. Lee, Y.C. Kang, D.W. Kang, J.S. Cho, Small 13 (2020) 2002213–2002226, https://doi.org/10.1002/smll.202002213.
[47] J.S. Lee, R. Saroha, S.H. Oh, D.H. Shin, S.M. Jeong, J.K. Kim, J.S. Cho, Small Methods 5 (2021) 2100195–2100209, https://doi.org/10.1002/smtd.202100195.
[48] S.H. Oh, S.M. Park, D.-W. Kang, Y.C. Kang, J.S. Cho, J Ind Eng Chem 83 (2020) 438–448, https://doi.org/10.1016/j.jiec.2019.12.017.
[49] R. Saroha, Y.H. Seon, B. Jin, Y.C. Kang, D.-W. Kang, S.M. Jeong, J.S. Cho, Chem. Eng. J. (2022), https://doi.org/10.1016/j.cej.2022.137141.
[50] J.S. Lee, R. Saroha, J.S. Cho, Nano-Micro Lett 14 (2022) 1–15, https://doi.org/10.1007/s40820-022-00795-8.
[51] R. Saroha, A.K. Panwar, J. Phys. D 50 (2017) 255501–255512, https://doi.org/10.1088/1361-6463/aa708c.
[52] Z. Li, L. Yuan, Z. Yi, Y. Liu, Y. Huang, Nano Energy 9 (2014) 229–236, https://doi.org/10.1016/j.nanoen.2014.07.012.
[53] Y. Jiang, X. Ma, J. Feng, S. Xiong, J. Mater. Chem. A 3 (2015) 4539–4546, https://doi.org/10.1039/C4TA06624C.
[54] D.B. Babu, K. Ramesha, Electrochim. Acta 219 (2016) 295–304, https://doi.org/10.1016/j.electacta.2016.10.026.
[55] S.-K. Park, J.-S. Park, Y.C. Kang, ACS Appl. Mater. Interfaces 10 (2018) 16531–16540, https://doi.org/10.1021/acsami.8b03104.
[56] B. Kalimuthu, K. Nallathamby, ACS Appl. Mater. Interfaces 9 (2017) 26756–26770, https://doi.org/10.1021/acsami.7b05103.
[57] R. Saroha, J.H. Oh, J.S. Lee, Y.C. Kang, S.M. Jeong, D.-W. Kang, C. Cho, J.S. Cho, Chem. Eng. J. 426 (2021) 130805–130818, https://doi.org/10.1016/j.cej.2021.130805.